Supplementary Information for strongly-anharmonic gateless gatemon qubits based on InAs/Al 2D heterostructure

Shukai Liu[1], Arunav Bordoloi[1], Jacob Issokson[2], Ido Levy[2], Maxim Vavilov[3], Javad Shabani[2], and Vladimir Manucharyan[1,4]

[1]Department of Physics, Joint Quantum Institute, and Quantum Materials Center, University of Maryland, College Park, MD, USA
[2]Center for Quantum Information Physics, Department of Physics, New York University, New York, NY, USA
[3]Department of Physics, University of Wisconsin-Madison, Madison, WI, USA
[4]Institute of Physics, Ecole Polytechnique Federale de Lausanne, Lausanne, Switzerland

Supplementary Information 1: Experimental setup

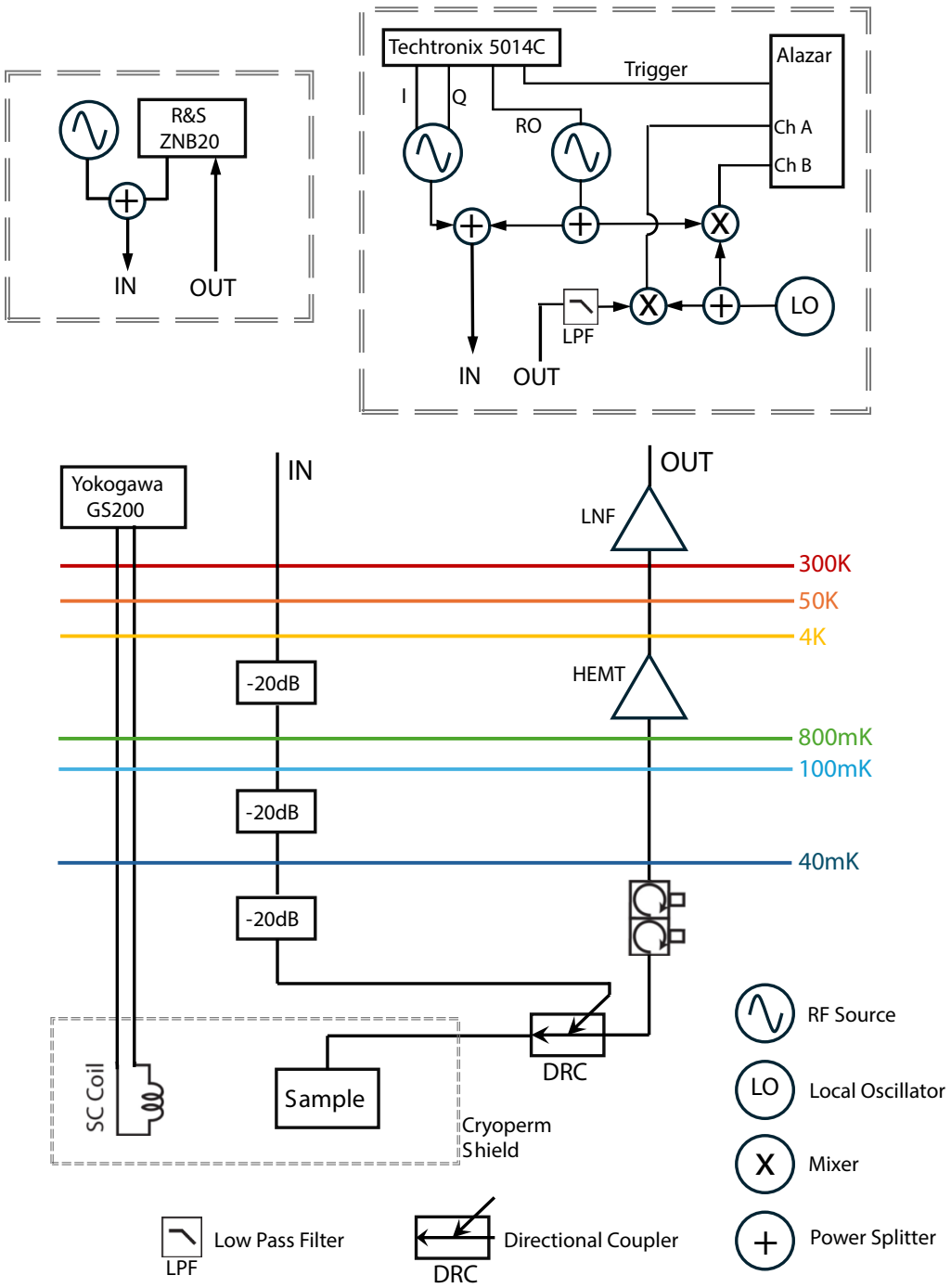

Supplementary Figure 1: Schematics of the experimental setup use for measuring the flux-tunable gatemon qubit.

Supplementary Information 2: One-Tone Spectroscopy

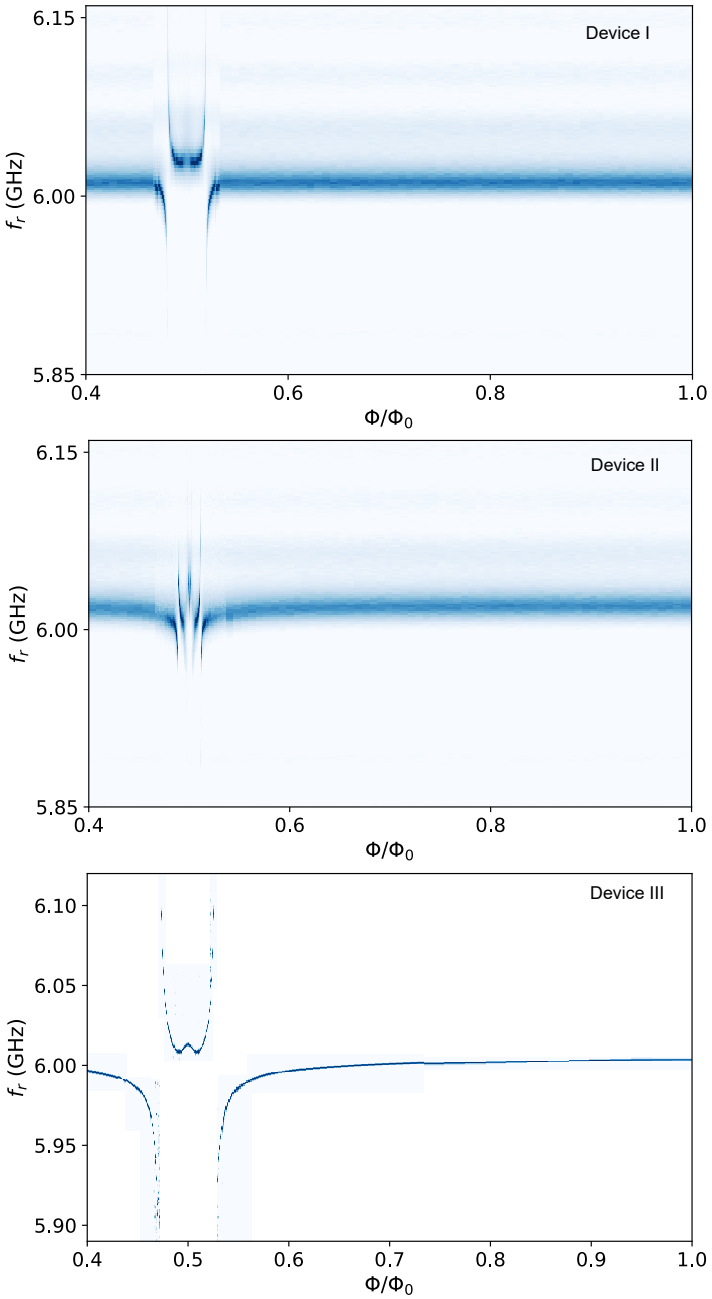

Supplementary Figure 2: One-tone spectroscopy showing $|S_{11}|$ as a function of the resonator drive frequency f_r and the applied external magnetic flux Φ/Φ_0 for device I, II and III, respectively. The resonator response exhibits a vacuum Rabi splitting with a cavity-qubit coupling strength of $g = 122\,\mathrm{MHz}$ for device I, $g = 101\,\mathrm{MHz}$ for device II and $g = 170\,\mathrm{MHz}$ for device III, respectively.

Supplementary Information 3: First-order flux insensitivity at $\Phi = 0.5\,\Phi_0$

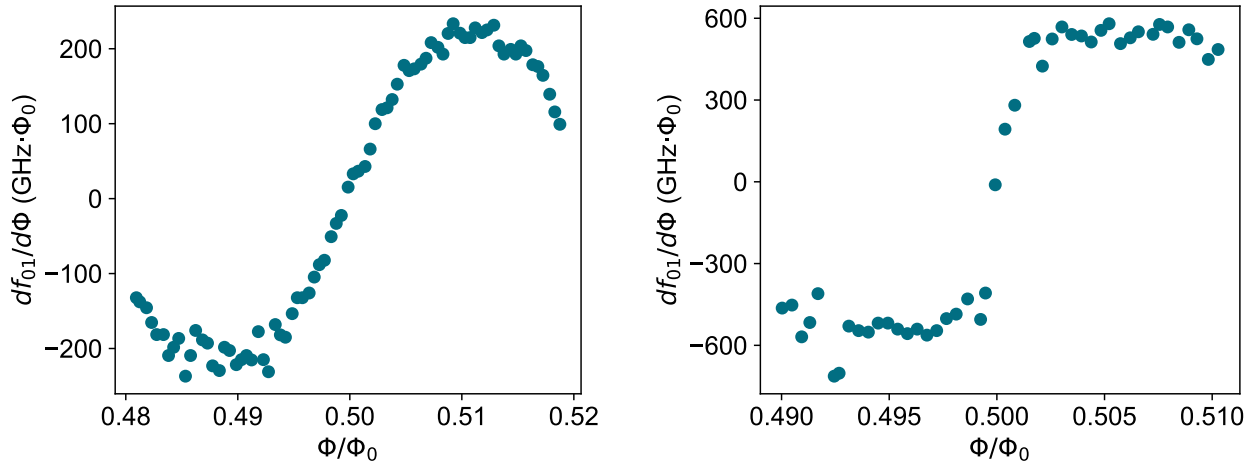

Supplementary Figure 3: Derivative of the $|0\rangle - |1\rangle$ transition qubit frequency $\mathrm{d}f_{01}/d\Phi$ as a function of the applied external magnetic flux Φ/Φ_0 for device I (left) and device II (right), indicating a first-order insensitivity to flux at the half-flux quanta $\Phi = 0.5\,\Phi_0$.

Supplementary Information 4: Charge-matrix elements

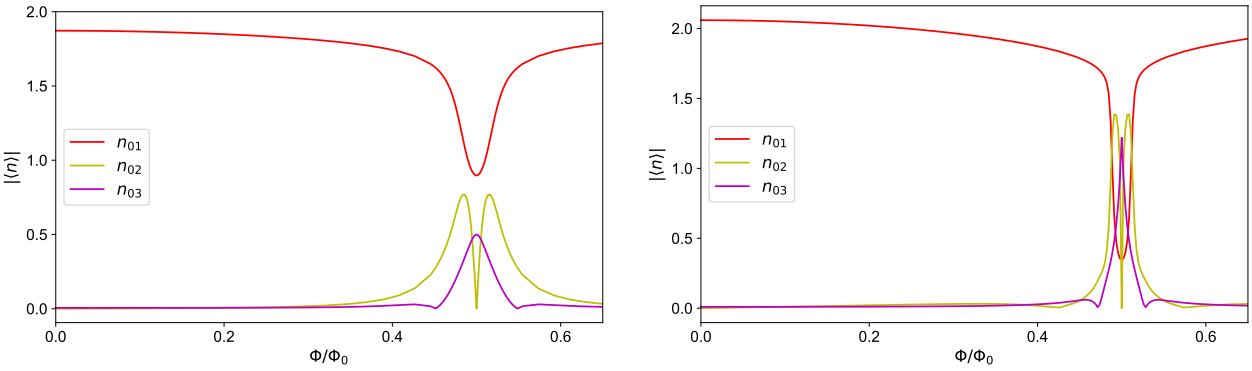

Supplementary Figure 4: Charge matrix elements vs flux Φ/Φ_0 for device I (left) and device II (right).

Supplementary Information 5: Higher-harmonic model comparison

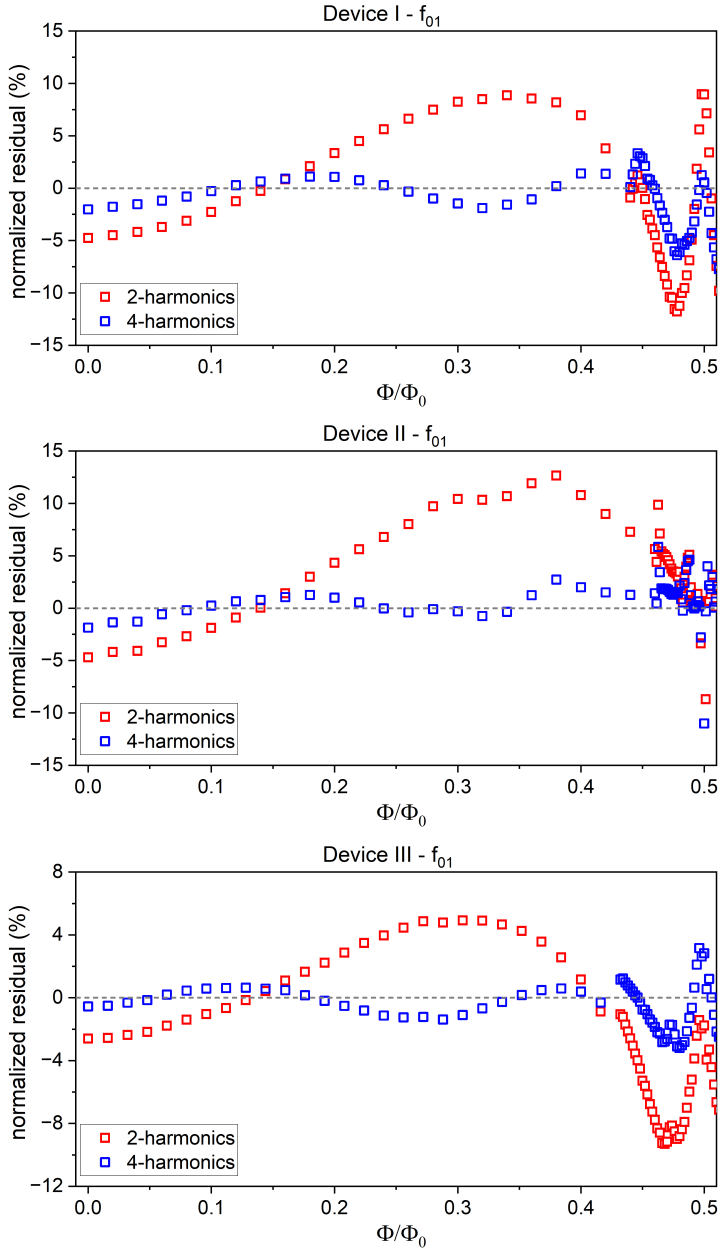

Supplementary Figure 5: Normalized residual $(f_{\mathrm{model}} - f_{\mathrm{meas}})/f_{\mathrm{meas}}$ as a function of Φ/Φ_0 for the $|0\rangle - |1\rangle$ qubit transition using the higher-harmonic model for device I, II and III, respectively. Here, k refers to the number of leading Fourier harmonic terms used to approximate the Josephson potential energy in $U = \sum_k E_{\mathrm{J}}^k \cos(k\varphi)$.

Supplementary Information 6: Multi-transparency model

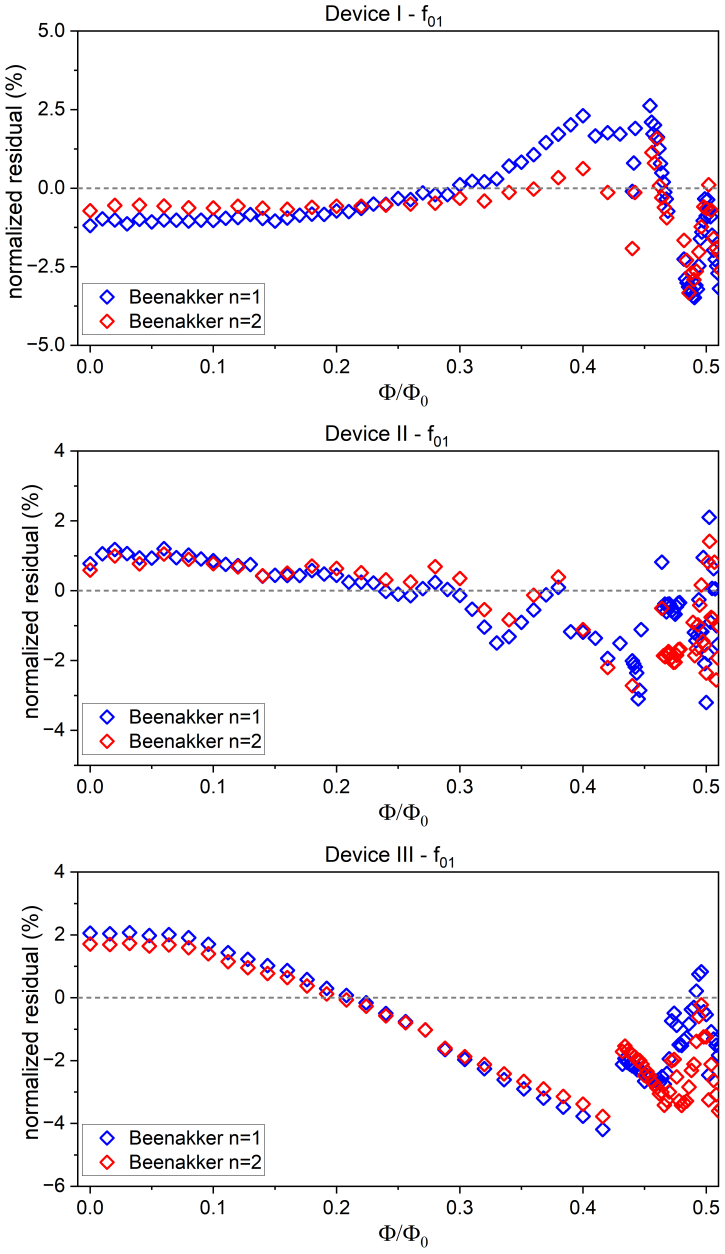

Supplementary Figure 6: Normalized residual $(f_{\text{model}} - f_{\text{meas}})/f_{\text{meas}}$ as a function of Φ/Φ_0 for the $|0\rangle - |1\rangle$ qubit transition using the single and multiple transparency model for device I, II and III, respectively. Here, n refers to the number of characteristic channel transparencies for each Josephson junction. We observe that increasing n from a single ($n = 1$) characteristic channel transparency to two ($n = 2$) channel transparencies does not lead to any significant reduction in the residuals.

Supplementary Information 7: T_1 flux dependence

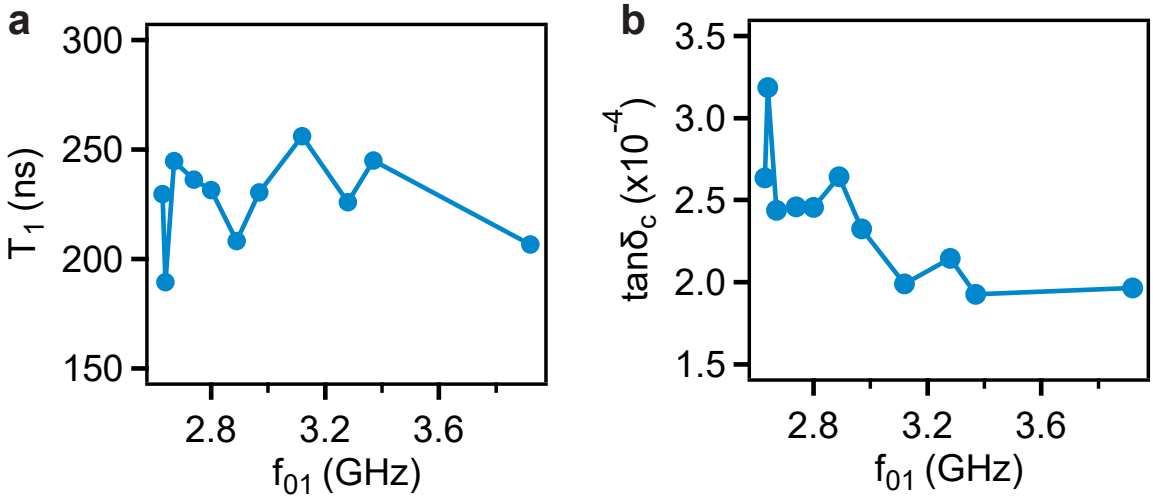

Supplementary Figure 7: **a.** T_1 as a function of the $|0\rangle - |1\rangle$ transition qubit frequency f_{01} in the vicinity of half-flux quanta $\Phi = 0.5\,\Phi_0$. **b.** The effective dielectric loss tangent $\tan\delta_c$ vs the qubit frequency f_{01} extracted from (**a**) using $\tan\delta_c = \frac{1}{T_1\omega_{01}}$, where $\omega_{01} = 2\pi f_{01}$.